Check for updates

Introducing functionalities into directly synthesised amorphous UiO-66-based metal–organic frameworks

Emily V. Shaw, [ID] [a] Javier Pérez-Carvajal, [ID] [b] Elena López-Elvira,[b] Shaoliang Guan,[ac] Timothy Lambden,[a] Georgina P. Robertson,[ad] Arad Lang,[ae] Joonatan E. M. Laulainen,[a] Celia Chen,[ac] Chumei Ye,[ac] Anna Herlihy,[f] Catherine Dejoie,[d] David A. Keen, [ID] [g] Paul Midgley,[a] Thomas D. Bennett*[ah] and Celia Castillo-Blas [ID] *[ab]

We report a scalable, water-based methodology for the direct room-temperature synthesis of porous amorphous UiO-66-type metal–organic frameworks (aMOFs), enabling the incorporation of a range of functionalised terepthalate linkers without organic solvents during framework formation. Powder X-ray diffraction and scanning electron diffraction confirm the formation of truly topologically amorphous UiO-66 derivatives, while pair distribution function (PDF) analysis shows that the amorphous frameworks retain the local structural motifs of their crystalline analogues despite the loss of long-range order. Relative to crystalline UiO-66, the directly synthesised amorphous UiO-66 exhibits a reduced but permanent porosity (BET surface area 286 $vs.$ 997 m^2 g^{-1} CO_2-accessible pore volume 0.196 $vs.$ 0.519 cm^3 g^{-1}), together with a high concentration of defects, consistent with a cluster : linker ratio of 1 : 5.3 compared with 1 : 6 for the ideal crystalline framework. In the esterification of levulinic acid, amorphous UiO-66 reaches 87.7% conversion to methyl levulinate after 3 h, compared with 75.5% for crystalline UiO-66, and retains 95% of its initial activity after five catalytic cycles ($vs.$ 86% for the crystalline analogue). These results demonstrate that direct, water-based synthesis provides access to functional, porous, and highly defective amorphous UiO-66 materials with catalytic performance comparable to or exceeding that of their crystalline counterparts under the conditions studied.

Introduction

Crystallinity is no longer a strict requirement in the field of metal–organic frameworks (MOFs). In recent years, amorphous MOFs (aMOFs), defined as disordered 3D hybrid materials lacking correlated long-range order beyond the core building blocks, have gained significant attention.[1,2] This interest stems from their enhanced chemical and thermal stability, improved processability, and inherently high defect concentrations, compared to their crystalline counterparts. These unique properties position aMOFs as promising candidates for a broad range of applications, including gas storage and separation,[3] drug delivery,[4] within electrochemistry (e.g. supercapacitors and electrochemical oxidation),[5,6] as well as catalysts and photocatalysts.[7,8]

To date, most aMOF materials have been obtained through post-synthetic amorphisation of their crystalline analogues, which results in the loss of correlated long-range order. This transition has typically been achieved using heat, pressure, chemical processes, mechanical stress or radiation.[9] These methods, however, provide limited control over the resulting structure and properties of the material, creating challenges in terms of reproducibility and design precision.[9] In addition, they often have a significant negative impact on the environment, as most crystalline materials are prepared using methanol, dimethylformamide (DMF) and other harmful solvents. Finally, the preparation of an aMOF via an intermediate crystalline phase is far less efficient in terms of both resources and time consumption than direct synthesis.

[a]Department of Materials Science & Metallurgy, University of Cambridge, 27 Charles Babbage Road, Cambridge, UK

[b]Instituto de Ciencia de Materiales de Madrid (ICMM-CSIC), Sor Juana Inés de la Cruz 3, 28049, Madrid, Spain. E-mail: castillo@icmm.csic.es

[c]Maxwell Centre, Cavendish Laboratory, University of Cambridge, J. J. Thomson Avenue, Cambridge, CB3 0HE, UK

[d]ESRF – the European Synchrotron Radiation Facility, CS 40220, Grenoble, Cedex 9, 38043, France

[e]Department of Materials Science and Engineering, Technion – Israel Institute of Technology, Haifa 3200003, Israel

[f]Diamond Light Source Ltd, Diamond House, Harwell Campus, Didcot, Oxfordshire, UK

[g]ISIS Facility, Rutherford Appleton Laboratory, Harwell Campus, Didcot, Oxfordshire OX11 0QX, UK

[h]School of Physical and Chemical Sciences, University of Canterbury, Private Bag 4800, Christchurch 8140, New Zealand. E-mail: thomas.bennett@canterbury.ac.nz
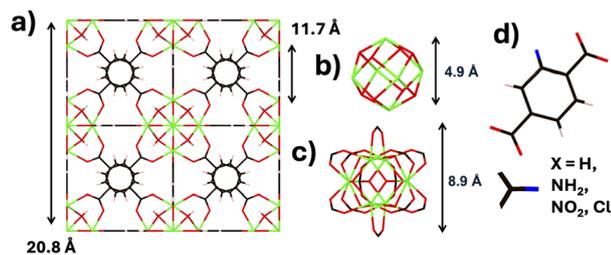
Fig. 1 Structure of UiO-66. (a) UiO-66 unit cell, (b) UiO SBU, defined as a $Zr_6O_4(OH)_4$ octahedra, (c) UiO node within the MOF structure; each octahedra coordinates 12 linkers, (d) terephthalic acid-based linker (x- BDC), where X = H, NH_2, NO_2 and Cl respectively. Structure calculated from a reported crystal structure.[18] Zirconium, oxygen and carbon are represented in green, red and black respectively, with potential functionality highlighted in blue. Hydrogens were omitted in a−c for clarity.

In recent years, direct synthesis has offered an emerging alternative, enabling the incorporation of disorder during framework formation.[10,11] This strategy allows for more controlled development of amorphous structures and facilitates tuneable properties, such as porosity, defect concentration and chemical functionality, through synthetic design. In addition, it expands the opportunity to fabricate MOF materials using more environmentally friendly procedures by the decreasing of solvent amount, minimising the amount of modulator, exchanging solvents such as DMF for greener alternatives, and decreasing the time and temperature of synthesis, which offers exciting avenues for the implementation of these materials in the industry.[12] Therefore, extending this approach opens new opportunities to apply reticular chemistry, traditionally reserved for crystalline materials, to amorphous frameworks.[13] Such expansion could lead to the development of functional materials with unique properties inaccessible *via* conventional crystallographic design. Above all, ensuring eco-friendly, cost- and resource-efficient synthesis is vital for the field's future.

UiO-type MOFs, Fig. 1, exhibit robust Zr_6-cluster secondary building units (SBUs), $Zr_6O_4(OH)_4$, *fcu* topology, and high coordination number, and thus, linker connectivity. Among the many MOF families, these present particularly promising candidates for exploring the direct synthesis of amorphous frameworks.[14] Their remarkable chemical robustness, structural versatility, and well-established crystalline synthetic protocols provide a strong starting point to develop amorphous analogues. Notably, a wide range of linker lengths and functionalities based on the fundamental terephthalic acid linker can be incorporated with minimal impact on the overall synthetic methodology,[15] which facilitates the development of water-based synthetic routes for a range of *a*UiO-based MOF materials. By adjusting these linker parameters, *a*MOFs could, theoretically, be precisely tailored in terms of pore size, surface area, and chemical functionality, and thus, tuning the properties and applications for these disordered materials.

Although the direct synthesis of amorphous UiO-66 materials has been previously demonstrated, systematic optimisation of these methods using readily available starting reagents

remains limited.[11,16] In this work, we address this gap by developing direct synthetic routes to a series of amorphous UiO-based MOFs without the requirement of preparing the Zr-based secondary building units (SBUs) prior to *a*MOF preparation. Specifically, we demonstrate the possibility of the universal applicability of this methodology of *a*Zr-MOF preparation through the direct synthesis of amorphous UiO-66 analogues by varying the identity of the linker incorporating functionalised terephthalic acid derivatives such as 2-aminoterephthalic acid (UiO-66-NH_2), 2-nitroterephthalic acid (UiO-66-NO_2), and 2-chloroterephthalic acid (UiO-66-Cl). This approach aims to expand the available synthetic strategies for designing disordered frameworks with tuneable structural and chemical properties for a broad range of applications. Crucially, all syntheses are performed under mild conditions using water as the reaction solvent, providing a more sustainable and accessible route to *a*MOFs. The resultant materials are characterised in terms of their structural disorder, porosity, and chemical functionality, to assess their suitability for targeted applications and to further understand the relationship between synthetic conditions, linker identity, and the properties of the resultant amorphous framework.

Discussion

Synthesis and characterisation of amorphous UiO-66 (*a*UiO-66)

A known water-based synthetic procedure to obtain a 'semi-crystalline' UiO-66 was adapted to develop a new greener synthetic route for the formation of an amorphous UiO-66 material, herein referred to as a_SUiO-66.[17]

This room temperature reaction occurred instantaneously, marked by the formation of a highly viscous opaque solution upon addition of the metal salt to the linker solution. This rapid gelation indicated fast nucleation kinetics, which could potentially maximise separation of nucleation and crystallisation stages, reducing the likelihood of forming mixed-phase products, a common issue reported in the literature.[9,16] The amorphous nature of a_SUiO-66 was confirmed by powder X-ray diffraction (PXRD), Fig. 2a and S1a, which exhibited three broad peaks, consistent with literature reports for *a*UiO-66.[16]
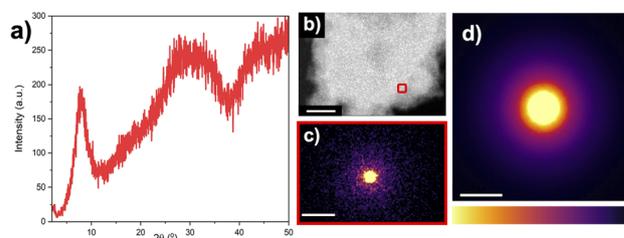

Fig. 2 (a) Powder X-ray diffraction pattern of a_SUiO-66, (b) virtual high-angle annular dark-field (HAADF) image of nanoparticle of a_SUiO-66, the red square notes the probed location of the diffraction pattern in (c). Scale bar = 200 nm. (d) Summed area diffraction maps of these crystals with scale bar = 2 nm^{-1}.
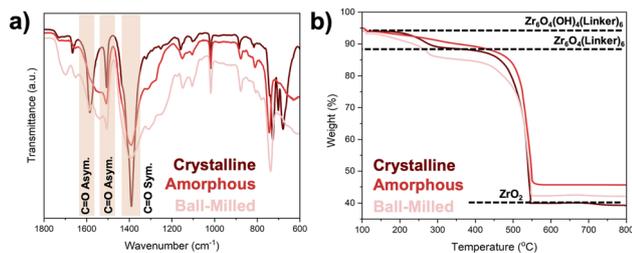
Fig. 3   (a) FT-IR spectra and (b) TGA data of UiO-66 (dark red), a_sUiO-66 (red) and a_mUiO-66 (light red).

Scanning electron diffraction (SED) further confirmed the absence of correlated long-range order. Individual sampling regions revealed no signs of local crystallinity, while area-averaged diffraction patterns displayed diffuse rings, Fig. 2. Through this, electron diffraction confirmed the sample as possessing a truly topologically amorphous structure, and confirmed the phase purity of the sample. Interestingly, heating of the intermediate gel form under solvothermal conditions revealed no change in the PXRD pattern, suggestive of the amorphous form possessing a degree of thermodynamic stability, Fig. S1b. Scanning electron microscopy (SEM) confirmed a significant decrease in particle size relative to the crystalline material, Fig. S2.

Fourier-transformed infrared spectroscopy (FTIR) confirmed the incorporation of the linker into the aMOF structure, with characteristic asymmetric C–O stretches at 1507 cm^{-1} and 1570 cm^{-1} and a symmetric stretch at 1390 cm^{-1}, consistent with crystalline UiO-66, Fig. 3a, S3 and Table S1.[19] The broadening of the carbonyl peaks indicated the disordered nature of a_sUiO-66. The emergence of a band at 1528 cm^{-1} was consistent with the presence of monocoordinated linker, and is consistent with bands developed in ball-milled UiO-66.[20] Overlapping of this band with the asymmetric C–O stretches, accounts for the coalescence of these peaks, resulting in a broad feature centred at ~1530 cm^{-1}.

Thermogravimetric analysis (TGA) was used to investigate thermal stability and linker binding. All samples – crystalline, a_mUiO-66 and a_sUiO-66 – showed similar TGA traces, with clear solvent loss (<100 °C), dihydroxylation, the loss of water from the SBU structure (~200 °C), and resultant thermal decomposition (~450 °C).[21] Isotherms were performed (Fig. S4) to identify the onset of thermal decomposition. Each sample showed early weight loss, likely due to the removal of monocoordinated or trapped uncoordinated linkers from the structure, which decomposes at lower temperatures. Thermal decomposition occurred at ~440 °C for all materials, demonstrating equivalent framework thermal stability. The gradual weight loss noted from 200–400 °C for a_sUiO-66 was attributed both to a high concentration of mono- and uncoordinated linkers within the structure, due to the disordered nature of the framework, as well as a high concentration of water bound to uncoordinated Zr-sites within the SBU structure. Energy dispersive X-ray spectroscopy (EDX), was used to investigate capping at uncoordinated sites, through the presence of Cl impurities, Fig. S5 and Table S2. This attributed roughly 1 wt% of the amorphous

sample to Cl$^-$ impurities from the ZrOCl$_2$ precursor, where they were not present in the crystalline material.

Metal-linker ratios were determined following methodology outlined by Abánades-Lázaro,[22] to indicate the concentration of uncoordinated metal defect sites, Table S3. For a_sUiO-66, assuming ideal Zr$_6$O$_4$(OH)$_4$ clusters, the cluster : linker ratio was determined as 1 : 5.3 versus 1 : 6 for the defect-free crystalline material. Given that water can act as a capping agent in Zr-MOF synthesis, introducing vacant sites into crystalline frameworks, it is likely that equivalent phenomena has occurred in the synthesis of a_sUiO-66.[23] In contrast to the crystalline form, a_sUiO-66 can reach a maximum cluster : linker ratio of 1 : 12, due to structural disorder allowing two metal sites to be capped by separate monocoordinated linkers, leaving free carboxylic acids. While these results suggest a high density of defects, further local structural analysis of SBU and linker coordination is required to confirm this.

X-ray total scattering $I(Q)$, collected at the I15-1 beamline (Diamond Light Source) was used to investigate the local structure (<8 Å) of a_sUiO-66 and crystalline UiO-66. Additionally, mechanically-amorphised UiO-66 (a_mUiO-66) was also explored as a comparison. The Bragg peak intensities present in the crystalline material were absent in a_sUiO-66, again consistent with its amorphous nature, according to structure factor, $S(Q)$, and $I(Q)$ data (Fig. S6). The pair distribution function (PDF) was extracted from the $S(Q)$ through the application of a Fourier Transform.[24] In this case, the $D(r)$ was utilised for the expression of the PDF as it maximises the relative intensities of long-range order peaks. Pair distribution functions were generated to investigate both the presence of long-range sample order, defined as order above ~8 Å, and the nature of the interactions which define the short-range order (SRO), Fig. 4a, S7 and Table S4. The short-range order (SRO) includes correlations both within the metal cluster and between the metal and linker. In both a_mUiO-66 and a_sUiO-66, the Zr$_6$ cluster is clearly distorted compared to its crystalline counterpart. Notably, peaks D and F, which correspond to Zr–Zr correlations within the cluster, are significantly diminished, indicating a pronounced disruption of the cluster structure. Such reductions in peak intensity are typical of distorted clusters and have been reported previously in the literature.[11,25] Nevertheless, based on the results from the ball-milled sample, we can confirm that the Zr$_6$O$_4$(OH)$_4$ cluster is preserved despite the high level of the distortion. The absence of significant peak intensity in the $D(r)$ beyond approximately 8
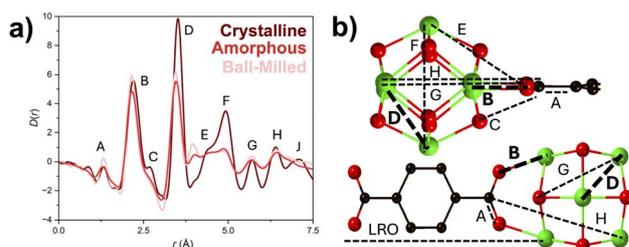

Fig. 4   (a) PDF Analysis of UiO-66 materials. The peak labels correspond to defined distances within the SBU, noted in (b).

Å further corroborates the disordered nature of these amorphous MOFs.

The PDF of both amorphous materials exhibit a shift in peak position for these key correlations, 2.18 Å (Zr–O) and 3.49 Å (Zr–Zr) to 2.11/2.13 Å and 3.40/3.38 Å, for a_sUiO-66 and a_mUiO-66 respectively, defined as peaks B and D, Fig. 4a. This shifting is suggestive of a slight compression or distortion of the Zr–SBU, whilst still maintaining the overall connectivity of the structure. Additionally, the broadening of peak C, located at 2.68 Å, would be consistent with a reduction in the rigidity of the SBU, producing a structure with slight variations in these correlation length scales. This variation could be expected from the changing synthetic conditions, as, within the crystalline synthesis, the $ZrCl_4$ precursors rapidly form the Zr-based SBU structures in the presence of DMF.[26] However, literature has also reported that $ZrOCl_2 \cdot 8H_2O$ has been observed to rapidly produce Zr-oxo clusters upon exposure to high concentrations of water.[27]

A decrease in relative intensity of several peaks (peaks C, D, F, G and H, located at 2.72 Å, 3.29 Å, 4.94 Å, 5.70 Å and 6.40 Å respectively) was noted. These were all found to contain contributions from Zr–C distances, suggestive of a lower coordination number compared to the crystalline material. This would be consistent with the presence of uncoordinated Zr-sites within the aMOF structure. This was supported by the increase in relative intensity of the Zr–O peak (peak B) compared to that of peak D, indicative of a high number of hydroxide capping groups present within the structure.

The largest structural distortions are noted in the 4–5 Å region of the plot, which observed a large increase in intensity localised at 4 Å, as well as a decrease in intensity at 4.96 Å, peak F compared to the crystalline material. The magnitude of the decrease in intensity at 4.96 Å is likely not entirely due to the reduction in Zr–C contributions. Instead, it is likely that the reduction in the Zr–O interactions as a result of the carbonyl group of the linker not binding to the metal. The noted potential distortion of the SBU structure of a_sUiO-66 likely propagates to the 4–5 Å region, resulting in an increased 'background' intensity at this length scale.

What is less clear however is the emergence of the peak centred at 4 Å in the amorphous material. This could also support a distortion across the Zr-based SBU, and is consistent with the compression-distortion noted by Ma *et al.* for a directly synthesised a_sZr-MOF.[11] This distortion of the node was confirmed by EXAFs (Extended X-ray Absorption Fine Structure), through changes to the relative peak intensities of the Zr–Zr peaks.[11] Additionally, the presence of monocoordinated ligands within the framework structure, confirmed through FTIR and TGA, will affect the PDF profile. Indeed, the flexible, dangling nature of these linkers would likely result in additional intensity in the longer-range of the local structure, resulting in variations in the short-range order whilst the SBU is largely equivalent. This is supported again by Ma *et al.*, where the observed changes in the PDF occurred after post-synthetic modifications, where both a decrease in coordination number, and a change in binding mode of the linker from di-to mono-coordinated were noted.[11]
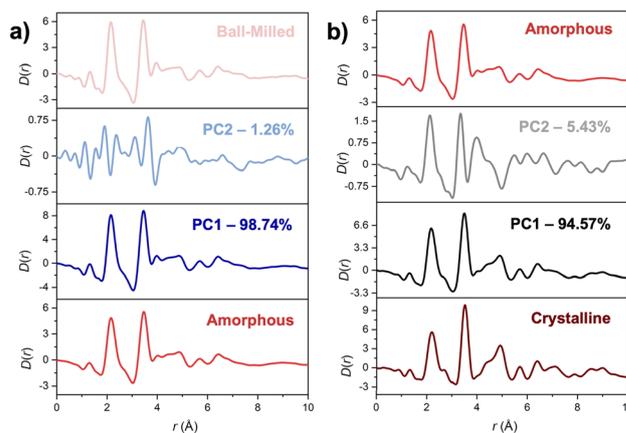

Fig. 5 Principal components extracted from comparison of (a) amorphous *vs.* ball-milled UiO-66 and (b) amorphous *vs.* crystalline UiO-66. Data were cropped at 10 Å. Amorphous corresponds to directly synthesised amorphous UiO-66.

Principal component analysis (PCA) was utilised to understand the extent of structural variation of the SRO.[10] PCA was performed both on a_mUiO-66 with a_sUiO-66, and a_sUiO-66 with UiO-66, Fig. 5a and b respectively. In both cases, PC1 represented an average of the structures, while PC2 showed how much the structures varied from each other. PCA of both amorphous UiO-66 PDF structures revealed minimal distortion between the two amorphous forms, with a contribution of 1.26%, indicating near equivalence in the structures. In contrast, PCA of crystalline UiO-66 and a_sUiO-66, 0–20 Å, revealed a greater structural distortion, Fig. S8, with a coefficient of 13.9%, due primarily to the loss of long-range order. PCA of cropped data, 0–10 Å, revealed a contribution of 5.43%, suggestive of minor variations in the local structure, Fig. 5 suggesting that most changes at the SRO are coming from the cluster distortions. Partial PDF spectra were generated from individual correlations for both the whole structure, and the SBU-isolated structure, Fig. S9, to better understand the nature of these variations. Comparison of the modelled SBU with the short-range order of a_sUiO-66 revealed potential minor distortions in the Zr_6 cluster, Fig. S10. Whilst the peaks corresponding to key Zr–Zr and Zr–O correlations were present, their peak positions and relative intensity varied from that associated with the crystalline material, demonstrated in PC2.

The synthetic method for a_sUiO-66 was modified by introducing a modulator, benzoic acid (50 equivalents), with the aim of slowing the rate of nucleation.[28] This effect was expected to occur through two mechanisms: first, by lowering the pH of the reaction solution, and second, by introducing a competing binding agent. By moderating nucleation in this way, it was hoped that the secondary building unit (SBU) structure could achieve a greater degree of order. Analysis of total scattering and PDF data (Fig. S11) revealed the presence of peaks beyond 8 Å, indicating that the sample retains a degree of long-range order. Interestingly, the peak intensities between 4–5 Å differed in intensity from those observed in both a_sUiO-66 and the crystalline material, with a significant peak present at 4 Å. This
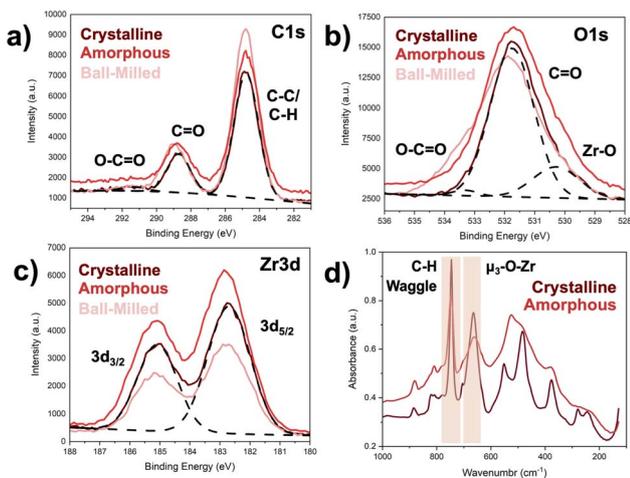
Fig. 6 XPS spectra of UiO-66 materials with deconvolutions labelled for the crystalline material, focusing on the (a) C 1s, (b) O 1s and (c) Zr 3d regions. (d) Far infrared spectroscopy of crystalline (dark red) and amorphous (bright red) UiO-66.

Fig. 7 (a) PXRD and (b) PDF analysis of local structure (<8 Å) of a_sUiO-66 (blue), a_sUiO-66-NH$_2$ (green), a_sUiO-66-NO$_2$ (orange) and a_sUiO-66-Cl (pink). Data were collected at (2 different beamtimes). (c) PCA analysis from the comparison of the a_sUiO-66-based MOFs with % variance values of 96.26 and 2.23% for PC1 and PC2 respectively. Eigenvalues were 3.85 and 0.09 respectively.

observation further suggests this feature cannot be attributed solely to the SBU distortion.

To investigate potential changes in the SBU further, X-ray photoelectron spectroscopy (XPS) was utilised, Fig. 6 and S12–15. XPS confirmed all UiO-66 samples preserved the Zr^{4+} oxidation state. Additionally, the positions of Zr 3d, O 1s and C 1s peaks remained largely unchanged across the UiO-66 materials, suggestive of retained chemical binding environments, Table S5.[29] Investigation as to the relative peak areas of these, indicating the number of these binding environments in the material, revealed changes between all three samples. Comparison of the relative area of the Zr 3d$_{5/2}$ peak observed a decrease in the number of Zr–O bonds for the a_sUiO-66 material, compared to the crystalline equivalent, likely due to the decreased carbonyl binding from reduced linker incorporation. This was supported through a reduction in relative peak area of the contributions associated with the linker. The lower magnitude of these decreases, 44% for Zr–O compared to 20% for C=O, O can be attributed to the presence of dangling monocoordinated linker within the structure, as suggested by TGA. Additionally, this could suggest some degree of reduction of Zr–O bonding within the SBU structure proving the presence of Cl coordinate to the Zr nodes, which could also explain the distortion or flexibility observed above. This confirms the distortions in the short-range order likely results from both the presence of monocoordinated linkers within the framework, as well as a distortion in the SBU structure, occurring during synthesis.

This was further investigated using far infrared spectroscopy (Far-IR), Fig. 6d, where broadening of the peaks localised <700 cm^{-1} was observed in the a_sUiO-66 material. Specifically, the broadening of the peak located at ~660 cm^{-1}, attributed to the μ_3-Zr–O stretch, confirmed disorder in the SBU structure.[30]

Variable linker in amorphous UiO-66 (aUiO-66-X)

Building on the successful preparation of a_sUiO-66, the synthetic approach was extended to a series of functionalised
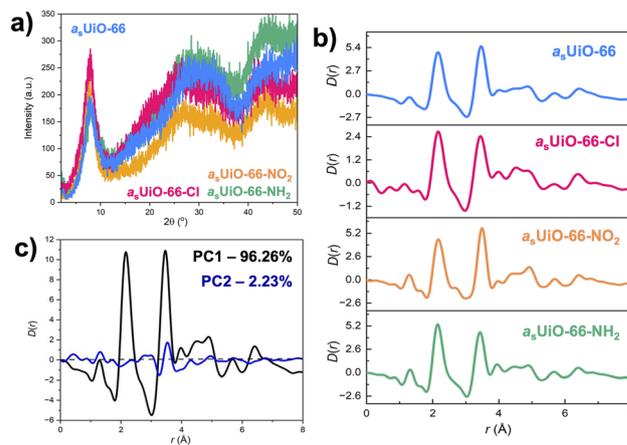
a_sUiO-66 using different functionalised terephthalic acids as linkers. Functionalisation of MOFs is a crucial strategy for tailoring their properties to specific applications, as it allows for precise control over characteristics such as chemical reactivity, selectivity, and stability.[31] For this study, a_sUiO-66-NH$_2$, a_sUiO-66-NO$_2$ and a_sUiO-66-Cl were synthesised, using 2-amino-terephthalic acid, 2-nitroterephthalic acid and 2-chloro-terephthalic acid respectively and equivalent synthetic conditions to the non-functionalised framework. The resultant aMOFs were characterised using PXRD, revealing equivalent traces to that of aUiO-66, with these samples denoted as a_sUiO-66-NH$_2$, a_sUiO-66-NO$_2$ and a_sUiO-66-Cl, Fig. 7a. Crystalline MOFs were prepared as comparison (Fig. S16). SEM again confirmed the amorphous MOFs nanoparticulate nature, Fig. S17.

The incorporation of linker into the aMOF structure was confirmed once again utilising FTIR, Fig. S18 and Table S8, noting the presence of equivalent peaks to that of the crystalline frameworks. The slight shift of the asymmetric stretch located at higher wavenumber was attributed to the presence of monocoordinated linker, often with a CO asymmetric stretch at lower wavenumber than the di-coordinated equivalent. The functionality of the linkers was retained upon formation of the aMOF, through the presence of a C–N, C–NH$_2$ based stretch at 1251 cm^{-1} and 1431 cm^{-1}, an NO$_2$ stretching vibration at 1534 cm^{-1} and a C–Cl vibration at 1051 cm^{-1}.[32–34] Broadening of the carbonyl peaks was observed, together with signals corresponding to monocoordinated linkers. Far-IR again confirmed broadening of the SBU-based stretches, consistent with disorder in the metal cluster structure, Fig. S19. The TGA results, similar to those of a_sUiO-66, showed equivalent T_d values for the disordered and crystalline materials, in addition to limited variation in SBU:linker ratios, Fig. S20 and Table S7. This, however, does not confirm the amorphous samples as possessing equivalent degrees of regular connectivity to that of

the crystalline material, as, as seen in the FTIR, a proportion of these linkers are likely monocoordinated, resulting in unbound metal sites. EDX determined higher wt% for the aMOFs, again consistent with the presence of unsaturated Zr sites. Fig. S21 and Table S8.

The equivalence of the structures formed were analysed using total scattering, Fig. S22 and PDF analysis, Fig. 7b and S23, with the no crystalline Bragg peaks identified in the total scattering. Investigation of the amorphous structures revealed no correlations at long length scale, consistent with the amorphous nature of these materials. Direct comparison of the PDF analysis of the aUiO-66-X materials revealed near-equivalent traces, however, variations were noted as to the relative intensity of the peaks located in the 4–5 Å region, as was noted in the comparison between a_s- and a_m-UiO-66.

Principle component analysis of the four a_sUiO-66-based materials revealed significant agreement between the disordered structures, with a low PC2 contribution of 2.23%, Fig. 7c. This suggested that the distortion of the functionalised a_sUiO-66 MOFs was analogous to that seen with a_sUiO-66 compared to the crystalline equivalent. As expected, the primary distortion was localised in the 4–5 Å region, suggesting that, whilst the structural distortion was present in all these materials, the absolute concentration of this distortion or structure defects varied across samples. This likely indicates that the nature of the defect or distortion is affected by the linker nature. This would indicate that the rate of linker binding, and subsequent coordination number of the linker, and di:monocoordination ratio is at least partially responsible for the observed structural shift.

Literature has noted that SBU-formation in UiO-66 crystalline synthesis occurs even prior to the addition of heat or linker solution, suggesting in this aMOF methodology, the SBU structure should have formed.[26] Additionally, this would suggest the linker nature should have limited effect on the degree of order the SBU holds within the structure. Indeed, the additional peak noted above, located at 4 Å, has been observed in an SBU-containing precursor solution utilised within literature, suggesting this feature could be as a result of an isolated, or low-coordination number SBU.[26] This is supported by work by Chen et al., which noted through computational modelling the preferential formation of a 'distorted' SBU structure, with near equivalence in the PDF to the short-range order reported here, with low linker coordination.[25]

Gas sorption of aUiO-66-X

Since the SBU connectivity is largely preserved, albeit with some structural distortion, the data suggest that these a_sMOF materials contain a high concentration of vacant metal sites. Such sites act as high-energy centres that are advantageous for a range of applications.[35] A key limitation of disordered MOFs produced by post-synthetic amorphisation is the near-complete loss of porosity, which restricts access to these defect sites.[9] In contrast, direct synthesis of aMOFs provides a route to highly defective, disordered materials that retain a degree of porosity comparable to their crystalline analogues, thereby making these defect sites more accessible and enhancing their potential utility.
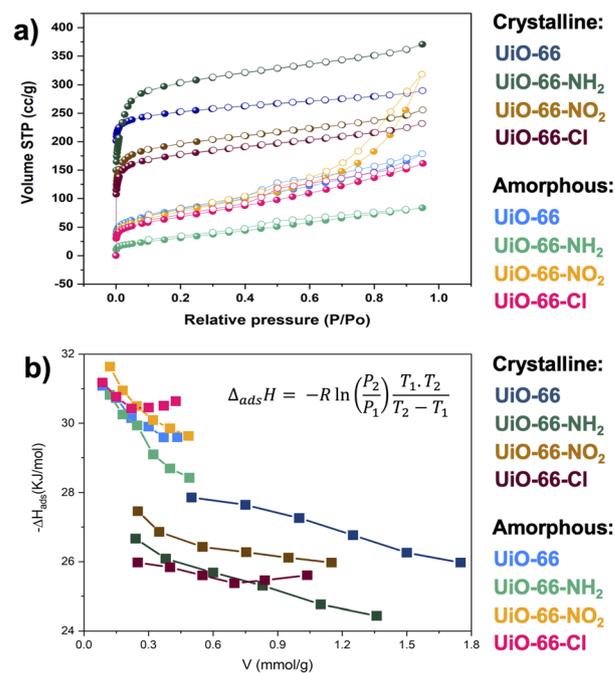
Fig. 8 (a) N_2 adsorption (filled points)/desorption (empty points) isotherms at 77 K show the lower surface area for the functionalised amorphous UiO-66 derivatives. (b) Isosteric heat of adsorption of all the materials (N = Surface coverage).

Gas sorption studies were conducted on these a_sMOF materials, to investigate if porosity was present in the disordered materials. This, coupled with the ability to introduce additional functionality into the linker, could result in the wide application of these materials.

N_2 and CO_2 adsorption isotherms (Fig. 8a and S24) revealed a pronounced decrease in sorption capacity for the amorphous materials compared to their crystalline counterparts, although a certain degree of porosity is retained. The BET surface area of a_sUiO-66 decreased to 286 m^2 g^{-1} compared to 997 m^2 g^{-1} for the crystalline material. Similarly, the total pore volume of accessible CO_2 follows this trend, decreasing from 0.5187 cm^3 g^{-1} to 0.1964 cm^3 g^{-1}. Whilst this represents a significant reduction, the synthetically amorphised material retains substantially higher porosity than most post-synthetically amorphised MOFs reported to date.[36] Comparison of this porosity to that reported in literature for other directly synthesised amorphous Zr-based MOFs revealed the samples in this study displayed equivalent, or improved, porosity compared to the literature, Table S9. Interestingly, a_sUiO-66-NH$_2$, a_sUiO-66-NO$_2$ and a_sUiO-66-Cl also exhibit permanent porosity in their amorphous states, as determined from the BET surface area extracted from the nitrogen adsorption measurements (Table 1). In these functionalised isoreticular structures, CO_2 remains partially accessible, although the observed trend deviates from that of UiO-66. The total accessible pore volume does not collapse completely, suggesting the persistence of ultramicropores (<0.7 nm) that contribute to the residual porosity of the amorphous frameworks (Fig. S25).

Table 1 Specific surface area (BET) and total pore volume of the amorphous MOF and its comparation with their typically crystalline counterparts

Sample	BET ($m^2\ g^{-1}$)	Total pore volume ($cm^3\ g^{-1}$)
UiO-66	997	0.5187
a_sUiO-66	286	0.1964
UiO-66-NH$_2$	1192	0.5644
a_sUiO-66-NH$_2$	120	0.1536
UiO-66-NO$_2$	746	0.3465
a_sUiO-66-NO$_2$	277	0.1698
UiO-66-Cl	682	0.3416
a_sUiO-66-Cl	243	0.1811

Isosteric heat of adsorption (ΔH_{ads}) was calculated from CO_2 isotherms following well documented procedures (see SI) for all samples (Fig. 8b and S26). Crystalline samples present lower ΔH_{ads} values than amorphous ones. This strongly suggest the presence of hydroxyl groups in the amorphous samples, which agrees with the high presence of defects observed by TGA and PDF data.[37]

Catalytic activity study of *a*UiO-66-X

The direct synthesis of *a*UiO-66-based MOFs provides materials with a high density of structural defects while retaining a degree of porosity. This combination is particularly attractive for catalysis, as it makes otherwise inaccessible defect sites available for reaction. Within these frameworks, two main types of catalytically active sites are introduced: Brønsted acid sites, arising from monocoordinated linkers with free carboxylic acid groups, and Lewis acid sites, associated with vacant Zr centres. The coexistence of these sites in high concentrations, together with the retained porosity and the use of water-based synthetic methods, positions these *a*MOFs as promising candidates for industrially relevant catalytic processes.

To evaluate their catalytic potential, the esterification of levulinic acid was selected as a model reaction. Levulinic acid, which can be derived from the breakdown of lignocellulosic biomass, is an important platform chemical and the precursor to value-added products such as alkyl levulinates and γ-valerolactone—compounds of growing interest in both the chemical and food industries. Previous studies have demonstrated that Lewis-active Zr sites in crystalline UiO-type MOFs catalyse this transformation efficiently, motivating the exploration of whether the higher concentration of accessible defect sites in amorphous analogues can further enhance performance.[38]

Harsh reaction conditions were chosen to probe, in addition to the activity of these MOFs, the chemical and thermal stability of the disordered frameworks compared to the crystalline materials. A control experiment was performed in the absence of catalyst, where gas chromatography (GC) revealed a yield of 41.8% and 33.8% for MeOH and EtOH respectively, with auto-catalysis attributed to the acidity of the levulinic acid, and the high temperatures, Fig. S27. Investigation of both crystalline and amorphous UiO-66 revealed conversions of 75.5% and 87.7% respectively after 3 h for the formation of methyl

levulinate. Conversion to ethyl levulinate was found to be higher for the crystalline material, relative to the amorphous material, 79.4% and 74.2% respectively. This decrease was attributed to a decrease in solvent diffusion through the pores due to the increased molecular size. For both reactions, the ball-milled material displayed lower conversion, likely due to the reduction in the porosity compared a_sUiO-66. No side products for these reactions were observed either through GC or NMR, Fig. S28, with NMR confirming the formation of the desired product.

The recyclability of the catalysts was then tested, with 5 catalytic cycles performed for each material. Esterification of levulinic acid to ethyl levulinate was chosen for this, as this reaction had a lower rate of autocatalysis, allowing more accurate probing into the effects of any catalyst degradation. Comparison of cycle 1 to cycle 5 revealed a decrease in catalytic activity of 13.9% and 5.2% for the crystalline and amorphous materials respectively, Fig. 9a. PXRD on the post-catalysis MOFs revealed a collapse of the crystalline structure, as well as a slight crystallisation of the amorphous material, with both forming equivalent structures, Fig. S29. Investigation of the progression of the change in structure revealed for both materials this occurred across multiple cycles. The crystalline framework lost the longer-range peaks as well as a loss of peak intensity, consistent with a decrease in sample order. The amorphous MOF revealed a splitting of the first diffraction feature, before an increase in both the peak intensity and sharpness. This is not unexpected, both due to the harsh conditions (high temperatures and low catalyst loading) as well as the presence of an acidic reagent likely resulting in the destabilisation of the structure. The decrease in catalytic activity for the crystalline material is likely due primarily to pore collapse, commonly seen as a result of crystallinity loss through chemical treatment.[39] The best-preserved activity for the amorphous is likely due to the macroporosity associated with the high missing-linker concentration, suggesting that, even in harsh conditions, the disordered nature of the material resists deactivation of the material.

The catalytic testing was then performed on the series of functionalised MOF materials, with the catalytic activity compared to that reported in the literature Fig. 9b and Table S10. This revealed near equivalent or increased catalytic activity
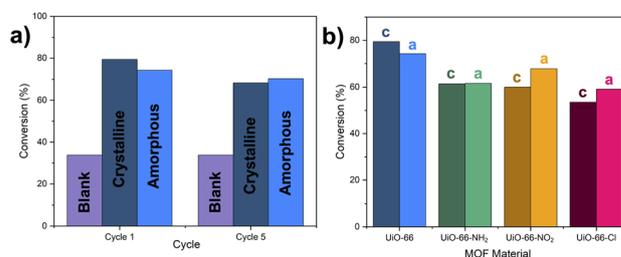

Fig. 9 (a) Conversion for the esterification of levulinic acid to ethyl levulinate for cycle 1 and cycle 5 of crystalline (dark blue) and amorphous (light blue) UiO-66, compared to the blank conversion (purple). (b) Conversion for the esterification of levulinic acid to ethyl levulinate, with a range of crystalline (dark) and amorphous (light) UiO-66-X materials. (X = H (blue), NH$_2$ (green), NO$_2$ (orange), Cl (pink)).

for all amorphous materials, compared to their crystalline equivalents. Investigation of the structures of the catalysts after 1 cycle revealed equivalent collapse/crystallisation that occurred with the UiO-66 materials, Fig. S30. The lower catalytic activity for –NO$_2$ and –Cl functionalised MOFs compared to the unfunctionalised material was unexpected, as the electron-withdrawing nature of the functional group should increase the Lewis acidity of the MOF. Interestingly, other studies into the comparative activity of UiO-66 and UiO-66-NH$_2$ observed higher activity for UiO-66-NH$_2$.[40] This variation from literature trends could be attributed to changes in relative defect concentrations, through increasing linker incorporation for functionalised MOFs, compared to unfunctionalised. Analysis of the resultant PXRD spectra after catalysis revealed a significant decrease in crystallinity of the functionalised materials, compared to UiO-66. This can likely be attributed to a higher intrinsic disorder in these substituted materials, destabilising the crystalline structure.

Total scattering data were collected for the samples after 5 cycles of catalysis, showing the 'crystalline' and 'amorphous' samples now displayed equivalent short- and long-range order, Fig. S31. Comparison to UiO-66 prior to catalytic testing revealed variance in both the local and extended structure. The change in the short-range order was found to be localised to the differences associated with the crystalline and amorphous UiO-66 MOF materials, albeit more extreme, Fig. S32. The emergence of the peak at 3.95 Å is consistent with the additional peak at ∼4 Å for a_sUiO-66. Additionally, the drop in peak intensity at ∼5 Å is also noted. Given this, as well as the shift of the Zr–O and Zr–Zr peaks to shorter length scales, 2.15 Å (Zr–O) and 3.42 Å (Zr–Zr), it is likely that heating under acidic conditions has induced both an increase in monocoordinated linkers, through the generation of defect sites (and thus, a more unstable structure), as well as a change in the SBU structure. Indeed, node distortion has been observed when heating crystalline UiO-66, resulting in the shifting of the short-range order peaks equivalent to that observed here.[41] The extended heating time, 3 h compared to 30 minutes, likely introduces significant SBU distortion, as well as providing the thermodynamic driving force for the sample to crystallise into a new structure, with comparison of the long-range order suggesting a different crystalline arrangement.

In addition to potential changes in the SBU structure, catalytic activity can be affected by the lability of the linkers,

resulting in the formation of intermediate active Zr-sites.[42] Given the high concentration of both missing-linker defects and monodentate/dangling linkers within the a_sUio-66 sample, as confirmed through TGA and FTIR, it is likely these can act cooperatively to increase the lability of the remaining linkers, and thus, the accessibility of Zr-sites.[43] Attempts were made to investigate the relative lability of the linker sites, through analysis of both crystalline and amorphous UiO-66 after heating at 80 °C for 3 hours in pure EtOH. TGA analysis was carried out to investigate any changes in the %weight loss associated with the linker. However, equivalent decreases in weight loss associated with linker decomposition were noted, Fig. S33a and b. Whilst this doesn't confirm an increase in linker lability for the amorphous MOFs, it is likely *in situ* studies or computational analysis would be needed to investigate this further.[44] Structural analysis of a_sUiO-66, Fig. S33c, heated at 80 °C in EtOH revealed limited change in the short-range order, suggestive of minimal metastable change in both linker binding and SBU structure. However, this does not preclude the existence of a transient intermediate structures that may rearrange upon cooling or upon exposure to ambient conditions. Importantly, heating of the amorphous sample alone did not result in any observable change in crystallinity, indicating that elevated temperature by itself is insufficient to drive structural reorganisation. These observations suggest that the formation of the thermodynamically stable phase likely requires the combined presence of levulinic acid and increased temperature.

The apparent pH (pH*) of these materials was also investigated following methodology by Cirujano *et al.*, in an MeOH solution to preserve the MOF binding, to qualitatively investigate the Brønsted acidity of the frameworks.[45] This revealed that all *a*MOF materials displayed a lower pH* compared to the crystalline frameworks, Fig. S34, attributed to a high concentration of monocoordinated linkers in the frameworks, potentially presenting interest for catalytic reactions requiring high Brønsted acidity.

Qualitative comparison of synthetic conditions

A qualitative comparison of the synthetic conditions used for amorphous and crystalline UiO-66 is provided in Table 2. The replacement of DMF, a toxic and environmentally hazardous solvent, with water has been highlighted as one of the major priorities for developing water-based MOF synthetic methods.[46] In addition, this amorphous MOF synthesis removes harsh

Table 2 Green considerations for the synthesis of amorphous and crystalline UiO-66

UiO-66	Amorphous	Crystalline
SOLVENT	Water	DMF
Metal precursor	$ZrOCl_2 \cdot 8H_2O$	$ZrCl_4$
Metal Salt : Linker (mmol)	1 : 1.5	1 : 2
Additive	$NaOH_{(aq)}$	$HCl_{(aq)}$
Synthesis temperature (°C)	20	180
PRESSURE	Ambient	Solvothermal
Synthesis time (h)	0.5	24
Atom economy (%)	89%	99%
DEMONSTRATED BATCH SCALE	Up to 5 g	Smaller-scale benchmarck synthesis
%Conversion-catalytic activity	74.2%	79.4%

acidic modulators, in this case HCl, from the synthetic method. A further goal for the development of greener synthetic methods is the reduction of temperature and pressure, both from an energy efficiency perspective, as well as for safety.[47] Since the amorphous material is synthesised at room temperature, and instantaneously, this significantly reduces the energy requirements of the experiment. These differences indicate a substantially lower process severity for the amorphous route in terms of solvent hazard, reaction temperature, and reaction duration.

The reduction in the safety and environmental concerns for the synthesis of aUiO-66, coupled with the equivalent, and at times improved, activity, compared to the crystalline material, could allow for these disordered materials to be utilised preferentially in industrial applications. Furthermore, the synthetic method for the production of amorphous MOFs has been demonstrated to be easily scalable, currently synthesising batches of 5 g, something proven to be challenging with crystalline MOFs.[48]

Conclusions

This work presents a new green and versatile approach for the direct synthesis of truly topologically amorphous UiO-66 MOFs with a range of functionalised linkers, with the analysis of this material summarised in Table S11. These materials lack correlated long-range order whilst largely retaining the local structure characteristic of their crystalline analogues. Linker analysis revealed a high concentration of missing-linker defect sites within the amorphous materials, compared to the crystalline MOFs, providing additional active sites for catalysis. The presence of a degree of permanent porosity within these disordered materials represents an opportunity for such aMOFs to be exploited in a range of applications in which they have not previously been employed, largely because this class of materials had not been taken into consideration.

The combination of defect sites and porosity for the disordered MOFs resulted in equivalent or enhanced catalytic performance for the esterification of levulinic acid, catalysed by Lewis acidic Zr^{4+} nodes. Recyclability testing also demonstrated enhanced catalyst stability for the disordered frameworks under harsh conditions, with a_sUiO-66 retaining 95% activity, compared to 86% for the crystalline framework.

The equivalent activity noted for the amorphous MOFs, coupled with the water-based, room-temperature synthetic methodology highlights the vast potential for these a_sUiO-66-based materials for its industrial development compared to conventional crystalline MOFs. Additionally, the noted ability to synthesise these a_sMOFs at increased scale potentially removes the most significant barrier to industrial applications of these materials. Future work will focus on utilising the synthetic tunability associated with crystalline MOFs to introduce alternative linker structures, as well as tune the resultant structure and properties of these a_sMOF materials.

Author contributions

C. C. B. and T. D. B. designed the project. E. V. S wrote the original manuscript with inputs from all authors. E. V. S.

preprepared and characterised the materials by PXRD, TGA and FTIR. Gas sorption collection and analysis was performed by J. P. C and E. L. E. TEM data was collected by J. E. M. L and P. A. M., with T. L. performing the analysis. Total scattering data were collected by E. V. S., G. P. R., A. L., C. C., J. S., C. Y. and D. A. K., and analysed by E. V. S with inputs from C. C. B and D. A. K. S. G. collected the XPS data. E. V. S performed the catalytic activity testing, under supervision of C. C. B.

Conflicts of interest

There are no conflicts to declare.

Data availability

The data supporting this article have been included as part of the supplementary information (SI) for scanning electron microscopy characterisation and catalysis tests. Supplementary information: data for this article, including electron microscopy, UV-VIS spectroscopy, pair distribution function and X-ray analysis, powder X-ray diffraction, liquid nuclear magnetic resonance, Fourier transformed infrared spectroscopy, gas sorption isotherms, thermal gravimetric analysis and X-ray photoelectron are available at Open Science Framework at DOI 10.17605/OSF.IO/GCDA7. See DOI: https://doi.org/10.1039/d5ta09975g.

Acknowledgements

Notes and references

1 T. D. Bennett and A. K. Cheetham, *Acc. Chem. Res.*, 2014, **47**, 1555–1562.
2 J. Fonseca, T. Gong, L. Jiao and H.-L. Jiang, *J. Mater. Chem. A*, 2021, **9**, 10562–10611.

3 A. F. Sapnik, C. W. Ashling, L. K. Macreadie, S. J. Lee, T. Johnson, S. G. Telfer and T. D. Bennett, *J. Mater. Chem. A*, 2021, **9**, 27019–27027.

4 C. Orellana-Tavra, E. F. Baxter, T. Tian, T. D. Bennett, N. K. H. Slater, A. K. Cheetham and D. Fairen-Jimenez, *Chem. Commun.*, 2015, **51**, 13878–13881.

5 J. Fonseca and S. Choi, *Catal. Sci. Technol.*, 2020, **10**, 8265–8282.

6 H. Wang, Q. Yang, N. Zheng, X. Zhai, T. Xu, Z. Sun, L. Wu and M. Zhou, *Nano Res.*, 2024, **20**(33), 2310702.

7 L. Liu, J. Zhang, X. Cheng, M. Xu, X. Kang, Q. Wan, B. Han, N. Wu, L. Zheng and C. Ma, *Nano Res.*, 2023, **16**, 181–188.

8 X. Zhang, H. Li, X. Lv, J. Xu, Y. Wang, C. He, N. Liu, Y. Yang and Y. Wang, *Chem.—Eur. J.*, 2018, **24**, 8822–8832.

9 E. V. Shaw, A. M. Chester, G. P. Robertson, C. Castillo-Blas and T. D. Bennett, *Chem. Sci.*, 2024, **15**, 10689–10712.

10 A. F. Sapnik, I. Bechis, A. M. Bumstead, T. Johnson, P. A. Chater, D. A. Keen, K. E. Jelfs and T. D. Bennett, *Nat. Commun.*, 2022, **13**, 2173.

11 N. Ma, S. Kosasang, J. Theissen, N. Gys, T. Hauffman, K. Otake, S. Horike and R. Ameloot, *Chem. Sci.*, 2024, **15**, 17562–17570.

12 C. Avci-Camur, J. Perez-Carvajal, I. Imaz and D. Maspoch, *ACS Sustain. Chem. Eng.*, 2018, **6**, 14554–14560.

13 O. M. Yaghi, *ACS Cent. Sci.*, 2019, **5**, 1295–1300.

14 J. H. Cavka, S. Jakobsen, U. Olsbye, N. Guillou, C. Lamberti, S. Bordiga and K. P. Lillerud, *J. Am. Chem. Soc.*, 2008, **130**, 13850–13851.

15 M. J. Katz, Z. J. Brown, Y. J. Colón, P. W. Siu, K. A. Scheidt, R. Q. Snurr, J. T. Hupp and O. K. Farha, *Chem. Commun.*, 2013, **49**, 9449.

16 F. Yang, W. Li and B. Tang, *J. Alloys Compd.*, 2018, **733**, 8–14.

17 J. M. Yassin, A. M. Taddesse and M. Sánchez-Sánchez, *Catal. Today*, 2022, **390–391**, 162–175.

18 Y. Ma, X. Han, S. Xu, Z. Wang, W. Li, I. da Silva, S. Chansai, D. Lee, Y. Zou, M. Nikiel, P. Manuel, A. M. Sheveleva, F. Tuna, E. J. L. McInnes, Y. Cheng, S. Rudić, A. J. Ramirez-Cuesta, S. J. Haigh, C. Hardacre, M. Schröder and S. Yang, *J. Am. Chem. Soc.*, 2021, **143**, 10977–10985.

19 V. V. Butova, V. R. Zdravkova, O. A. Burachevskaia, A. A. Tereshchenko, P. S. Shestakova and K. I. Hadjiivanov, *Nanomaterials*, 2023, **13**, 1675.

20 Z. Su, Y.-R. Miao, G. Zhang, J. T. Miller and K. S. Suslick, *Chem. Sci.*, 2017, **8**, 8004–8011.

21 A. Schaate, P. Roy, A. Godt, J. Lippke, F. Waltz, M. Wiebcke and P. Behrens, *Chem.—Eur. J.*, 2011, **17**, 6643–6651.

22 I. A. Lázaro, *Eur. J. Inorg. Chem.*, 2020, **2020**, 4284–4294.

23 K. Tan, H. Pandey, H. Wang, E. Velasco, K.-Y. Wang, H.-C. Zhou, J. Li and T. Thonhauser, *J. Am. Chem. Soc.*, 2021, **143**, 6328–6332.

24 D. A. Keen, *Crystallogr. Rev.*, 2020, **26**, 143–201.

25 Z. Chen, G. D. Stroscio, J. Liu, Z. Lu, J. T. Hupp, L. Gagliardi and K. W. Chapman, *J. Am. Chem. Soc.*, 2023, **145**, 268–276.

26 H. Xu, S. Sommer, N. L. N. Broge, J. Gao and B. B. Iversen, *Chem.—Eur. J.*, 2019, **25**, 2051–2058.

27 B. Bueken, N. Van Velthoven, T. Willhammar, T. Stassin, I. Stassen, D. A. Keen, G. V. Baron, J. F. M. Denayer, R. Ameloot, S. Bals, D. De Vos and T. D. Bennett, *Chem. Sci.*, 2017, **8**, 3939–3948.

28 S. L. Griffin, M. L. Briuglia, J. H. ter Horst and R. S. Forgan, *Chem.—Eur. J.*, 2020, **26**, 6910–6918.

29 X. Fang, S. Wu, Y. Wu, W. Yang, Y. Li, J. He, P. Hong, M. Nie, C. Xie, Z. Wu, K. Zhang, L. Kong and J. Liu, *Appl. Surf. Sci.*, 2020, **518**, 146226.

30 X. Zhang, Y. Yang, X. Lv, Y. Wang, N. Liu, D. Chen and L. Cui, *J. Hazard. Mater.*, 2019, **366**, 140–150.

31 S. Biswas and P. Van Der Voort, *Eur. J. Inorg. Chem.*, 2013, **2013**, 2154–2160.

32 L. Huo, J. Li, L. Wang, S. Zhang, Y. Pu, C. Zhai, C. Qiao and S. Zhou, *ChemistrySelect*, 2025, **10**(23), e04044.

33 P. An, F. Zhu, S. Liu, X. Zhou, C. Wang, Y. Liu, H. Meng and X. Zhang, *Appl. Biochem. Biotechnol.*, 2022, **194**, 5167–5184.

34 Z. Wang, Y. Jia, W. Song, X. Li, K. Xu and Z. Wang, *J. Clean. Prod.*, 2021, **300**, 126974.

35 S. Daliran, A. R. Oveisi, C.-W. Kung, U. Sen, A. Dhakshinamoorthy, C.-H. Chuang, M. Khajeh, M. Erkartal and J. T. Hupp, *Chem. Soc. Rev.*, 2024, **53**, 6244–6294.

36 L. N. McHugh and T. D. Bennett, *J. Mater. Chem. A*, 2022, **10**, 19552–19559.

37 G. C. Shearer, S. Chavan, S. Bordiga, S. Svelle, U. Olsbye and K. P. Lillerud, *Chem. Mater.*, 2016, **28**, 3749–3761.

38 D. A. Bravo Fuchineco, A. C. Heredia, S. M. Mendoza, E. Rodríguez-Castellón and M. E. Crivello, *ChemEngineering*, 2022, **6**, 26.

39 Y. Feng, M.-Y. Zou, H.-C. Hu, W.-H. Li, S.-L. Cai, W.-G. Zhang and S.-R. Zheng, *Chem. Commun.*, 2022, **58**, 5013–5016.

40 F. G. Cirujano, A. Corma and F. X. Llabrés i Xamena, *Catal. Today*, 2015, **257**, 213–220.

41 S. M. Vornholt, Z. Chen, J. Hofmann and K. W. Chapman, *J. Am. Chem. Soc.*, 2024, **146**, 16977–16981.

42 R. A. Peralta, P. Lyu, A. López-Olvera, J. L. Obeso, C. Leyva, N. C. Jeong, I. A. Ibarra and G. Maurin, *Angew. Chem., Int. Ed.*, 2022, **61**, e202210857.

43 J. Hajek, C. Caratelli, R. Demuynck, K. De Wispelaere, L. Vanduyfhuys, M. Waroquier and V. Van Speybroeck, *Chem. Sci.*, 2018, **9**, 2723–2732.

44 R. A. Peralta, M. T. Huxley, P. Lyu, M. L. Díaz-Ramírez, S. H. Park, J. L. Obeso, C. Leyva, C. Y. Heo, S. Jang, J. H. Kwak, G. Maurin, I. A. Ibarra and N. C. Jeong, *ACS Appl. Mater. Interfaces*, 2023, **15**, 1410–1417.

45 F. G. Cirujano and F. X. Llabrés i Xamena, *J. Phys. Chem. Lett.*, 2020, **11**, 4879–4890.

46 E. R. Engel and J. L. Scott, *Green Chem.*, 2020, **22**, 3693–3715.

47 H. Reinsch, *Eur. J. Inorg. Chem.*, 2016, **2016**, 4290–4299.

48 T. Paul, A. Juma, R. Alqerem, G. Karanikolos, H. A. Arafat and L. F. Dumée, *J. Environ. Chem. Eng.*, 2023, **11**, 111112.

49 A. Fitch, C. Dejoie, E. Covacci, G. Confalonieri, O. Grendal, L. Claustre, P. Guillou, J. Kieffer, W. de Nolf, S. Petitdemange, M. Ruat and Y. Watier, *J. Synchrotron Radiat.*, 2023, **30**, 1003–1012.

50 C. Chen, A. Lang and E. V. Shaw, *Towards Stable Binary Hybrid Perovskite Glasses: A Combined Long- and Short-Range Order Structural Study*, 2028, DOI: 10.15151/ESRF-ES-2037546702.